Universiteit Leiden
The Netherlands

Dusty perspectives on the cradles of planets
Guerra Alvarado, O. M.

From large-scale outflows to compact line emission in IRAS4A2

Osmar M. Guerra-Alvarado, N. van der Marel, P. Nazari, J. Di Francesco, Ł. Tychoniec, L. W. Looney, E. G. Cox, D. J. Wilner, M. R. Hogerheijde.

Abstract

Aims. Studying protostellar objects in their earliest stages, particularly during the Class 0 phase, provides key insight into the beginnings of planet formation and dust evolution. Disentangling the various components, such as the envelope, outflow, and nascent disk, to characterize and understand these young systems, however, is particularly challenging. High spatial and spectral resolution observations of molecular line emission with the Atacama Large Millimeter/submillimeter Array (ALMA) are therefore crucial for probing their complex environments.

Methods. In this work, we present high-resolution ALMA observations of the IRAS4A2 Class 0 system. We analyze the gas emission surrounding this young source, tracing it from the extended outflow to the most compact inner region and identifying emission lines using the spectral analysis tool CASSIS.

Results. We detected large, well-traced outflows in HCN, H_2CO, and HCO^+, as well as numerous complex organic molecules (COMs) within the system. Using moment maps, we analyzed the kinematics and spatial distributions of these molecules, finding that the emission spans a wide range of spatial scales, from large-scale outflows to compact regions within the IRAS4A2 core, with some molecular lines showing signatures of Keplerian rotation. In contrast, the primary IRAS4A1 exhibits little to no molecular emission, likely due to the strong absorption of the optically thick dust around it.

Conclusions. Our results indicate that the IRAS4A2 system consists of multiple components that are traced by different molecules. Most complex molecules seem to trace a warm inner envelope closer to the central star, while S-bearing molecules and outflow tracers follow a more extended layer with lower upper energy states around IRAS4A2. On the contrary, certain molecules exhibiting both extended and compact emission appear to trace multiple components or structures simultaneously, which suggests a more complex spatial distribution and chemical stratification

within IRAS4A2.

3.1 Introduction

Studying and understanding the evolution of protoplanetary disks from very embedded Class 0 objects to Class II disks is fundamental to unraveling the processes of planet formation. Protoplanetary disks emerge at very early evolutionary stages (Jørgensen et al. 2009; Harsono et al. 2014; Maury et al. 2019; Tobin et al. 2020), with evidence that suggests that planet formation may already be underway during these initial phases (Harsono et al. 2018; Tychoniec et al. 2020). Although many of these early-stage disks appear smooth in current observations (Hsieh et al. 2024), substructures such as rings, gaps, and spirals could already be forming but remain undetected or hidden due to resolution limitations, optical depth effects (Ohashi et al. 2023) and temperature effects (Nazari et al. 2025). Even though studying planet formation in Class 0/I sources remains a challenge, primarily because of the optically thick dust continuum emission, it is still possible to study the chemical composition of these young disks, which can provide crucial insights into their evolution.

In this context, numerous Class 0/I protostars have been identified with hot, dense environments known as hot corinos, which are analogs of the hot cores found in high-mass star-forming regions (Ceccarelli 2004). Many of these sources have been found to contain high abundances of Complex Organic Molecules (COMs), species with six or more atoms (Herbst & van Dishoeck 2009; Caselli & Ceccarelli 2012; Ceccarelli 2023). Most of these studies, however, have been conducted at low spatial resolution, limiting our ability to resolve the detailed structure and stratification of molecular species within these young disks.

With the unprecedented sensitivity and resolution of the Atacama Large Millimeter/submillimeter Array (ALMA) we are now able to investigate in more detail the molecular distribution of these hot corinos.

As of today, only a handful of Class 0 hot corino sources have been resolved at high angular resolution ($\sim 0.1"$) (IRAS 16293-2422 A (Maureira et al. 2022), SVS13-A (Bianchi et al. 2022), B335 (Okoda et al. 2022),

IRAS4A2 (Frediani et al. 2025), HH212 (Lee et al. 2022)) and L1448-mm
(Nazari et al. 2024). Interestingly, in HH 212, Lee et al. (2022) revealed
molecular stratification, which was attributed to the binding energies of
the molecules (sublimation temperature), as the temperature is expected
to increase closer to the host star. Studying these young protoplanetary
disks, where molecules sublimate at specific temperatures in different
regions, can provide insights into where planet formation and dust growth
may already be occurring, which we aim to identify in IRAS4A2.

IRAS4A2 was identified as the second hot corino source ever by Bot-
tinelli et al. (2004). It is located at a distance of 293 pc (Zucker et al. 2018)
in the NGC1333 region in Perseus, and it is part of a binary Class 0 sys-
tem, separated by 1.8" from its primary component, IRAS4A1 (Tobin et al.
2018). IRAS4A2 has been extensively studied before (Taquet et al. 2015;
López-Sepulcre et al. 2017; De Simone et al. 2017), identifying several
complex organic molecules and well-characterized outflows (Santangelo
et al. 2015).

In this work, we present a detailed study of the IRAS4A2 hot-corino,
from its large-scale outflows to its innermost compact emission. In Sec-
tion 3.2, we describe the observations and the process to obtain the spec-
tral line emission. Section 3.3 discusses our line identification method,
along with the techniques used to create the images of the outflows and
the extended and compact emission. Finally, in Section 3.4, we explore
the possible spatial distribution of these molecules and their implications
for IRAS4A2 in the context of dust, disk evolution, and planet formation.

3.2   Observations

The spatially resolved line observations for IRAS4A2 were obtained us-
ing the Atacama Large Millimeter/submillimeter Array (ALMA). Specif-
ically, Band 4 and Band 6 data were gathered under the project code
2018.1.00510.S (PI: James Di Francesco). For a more comprehensive un-
derstanding of the observations, including details about data characteris-

tics, calibration, self-calibration, and imaging of the continuum emission, refer to Guerra-Alvarado et al. (2024)

Line spectral windows were separated from the continuum ones, and in this instance, no channel averaging was applied. The self-calibration tables were derived from the continuum analysis and subsequently used in the line spectral windows. In Band 6, observations were carried out using two spectral windows, which we refer to as O6B1 and O6B2 for simplicity. O6B1 has a rest frequency of 267.557 GHz and encompasses two spectral windows (SPWs), each featuring 960 channels. These SPWs have central frequencies of 267.568 GHz and 267.569 GHz, respectively. O6B2, on the other hand, has a rest frequency of 265.886 GHz with four SPWs, each with 960 channels and central frequencies of 265.874 GHz, 265.894 GHz, 265.896 GHz, and 265.898 GHz, respectively. In total, the Band 6 data of O6B1 and O6B2 cover frequency ranges from 265.8214 GHz to 265.9385 GHz and from 267.4925 GHz to 267.6103 GHz, respectively.

The Band 4 line data have a rest frequency of 140.839 GHz with two SPWs, each containing 1920 channels with a central frequency of 140.795 GHz and a frequency range between 140.7319 - 140.8512 GHz. Across all observations, the system velocity was assumed to be 6.95 km/s (Di Francesco et al. 2001), which was later used for the analysis.

The final data cubes were produced using the *tclean* task in CASA, with *specmode* set to "cube" and the deconvolver to "Multiscale." We used scale values of 0, 2.5, 10, and 20 times the pixel size, which was fixed at 0.02" for all line cubes, approximately ten times smaller than the beam size. The spectral resolution is 0.5 for Band 6 observations and 1 for Band 4. These values were selected to balance sensitivity with maintaining the highest possible spectral resolution. Briggs weighting with a robust parameter of 0.5 was adopted for both datasets, as it was found to be the optimal choice based on the cubes images and also in the continuum images presented in Guerra-Alvarado et al. (2024). It also provided the best resolution against other robust values for determining the spatial distribution of the molecular emission, without blurring or

Table 3.1: Data cubes characteristics

Observations	Rest Frequency (GHz)	Beam Size (")	Channel Width (km s^{-1})	RMS (mJy beam^{-1})
O6B1 short baseline	267.557	0.28 × 0.17	0.5	2.8
O6B2 short baseline	265.886	0.28 × 0.17	0.5	2.87
Band 4 short baseline	140.839	0.44 × 0.28	1	2.3
O6B1 long+short baseline	267.557	0.13 × 0.085	0.5	1.59
O6B2 long+short baseline	265.886	0.155 × 0.10	0.5	1.57
Band 4 long+short baseline	140.839	0.10 × 0.047	1	0.95

missing any large-scale structures or weaker lines. This approach was
confirmed through comparison with images made via natural weighting.
The final characteristics are shown in Table 3.1 with typical beam sizes of
0.1" and rms values of ~1 mJy/beam per 1 km/s channel.

Finally, for the short baseline data, continuum subtraction was per-
formed prior to imaging using the *uvcontsub* task in CASA, resulting in
three short baseline cubes. For the concatenated data, which has higher
resolution and greater sensitivity to small features, determining the con-
tinuum level was more challenging. To enhance the accuracy of contin-
uum subtraction and better determine the continuum emission in the
image cubes, the STATCONT tool Sánchez-Monge et al. 2018 was em-
ployed. STATCONT utilizes a 'corrected sigma-clipping algorithm' for
determining continuum emission in line-rich sources like IRAS4A2. This
method was applied to all concatenated cubes in the study, resulting in
the creation of three other cubes. We used only the short-baseline data
to account for the most extended emission, to study the large-scale out-
flows, and the concatenated (short plus large baseline) data to study the
emission surrounding IRAS4A2.

3.3 Results

3.3.1 Analysis and line detection with CASSIS

We conducted an exploration of the spectral emission windows within
the concatenated cubes and identified several emission lines originat-
ing from a small region near the center of IRAS4A2. Spectra from all of

our data were extracted within CARTA (Cube Analysis and Rendering Tool for Astronomy) (Comrie et al. 2018) by selecting a pixel as close as possible to the continuum peak, but still outside the region affected by absorption, located at Dec = 31:13:31.9791986 and RA = 3:29:10.4336922. Subsequently, these spectra were converted into brightness temperature and processed for analysis using the CASSIS spectral analysis tool version 5.1.1 (Vastel et al. 2015). Following the methodology outlined in Nazari et al. (2022), we assumed local thermodynamic equilibrium (LTE) conditions and employed a fitting-by-eye approach. Potential transitions were investigated within CASSIS, utilizing the Cologne Database for Molecular Spectroscopy (CDMS, Müller et al. (2001)) and the Jet Propulsion Laboratory (JPL) database (Pickett et al. 1998).

Commonly detected molecules and COMs were prioritized in the search, with upper energy state levels and Einstein coefficient limits set to $E_{up} \leq 800$ K and $A_{ul} \geq 9 \times 10^{-6}$ s^{-1}. Since we extracted the spectra from single pixels, the source size parameter in CASSIS was uniformly set to 1000 for all lines, i.e., no non-unity beam filling factors were assumed. The Full Width at Half Maximum (FWHM) of each line was adjusted to fit the spectra better, and the V_{lsrk} was uniformly set to 6.95 km/s for all spectral cubes.

Our data revealed emission lines from SO_2, OCS, HCN, and H_2CO, along with several COMs (see Table A.1). These emission lines exhibit a variety of spatial components and kinematic structures. In the following section, we first describe the identification of the emission lines around IRAS4A2, we then characterize the spatial distribution of the integrated emission and analyze the kinematics, beginning with the outflow, followed by the extended emission, and concluding with the compact COM emission.

Following the criteria from (Pickett et al. 1998), a molecule was considered detected if at least three lines were found at 3-σ; otherwise, it was categorized as a 'tentative detection'. Figure 3.1 displays the observed spectra, where lines were identified, from our cubes in IRAS4A2 alongside
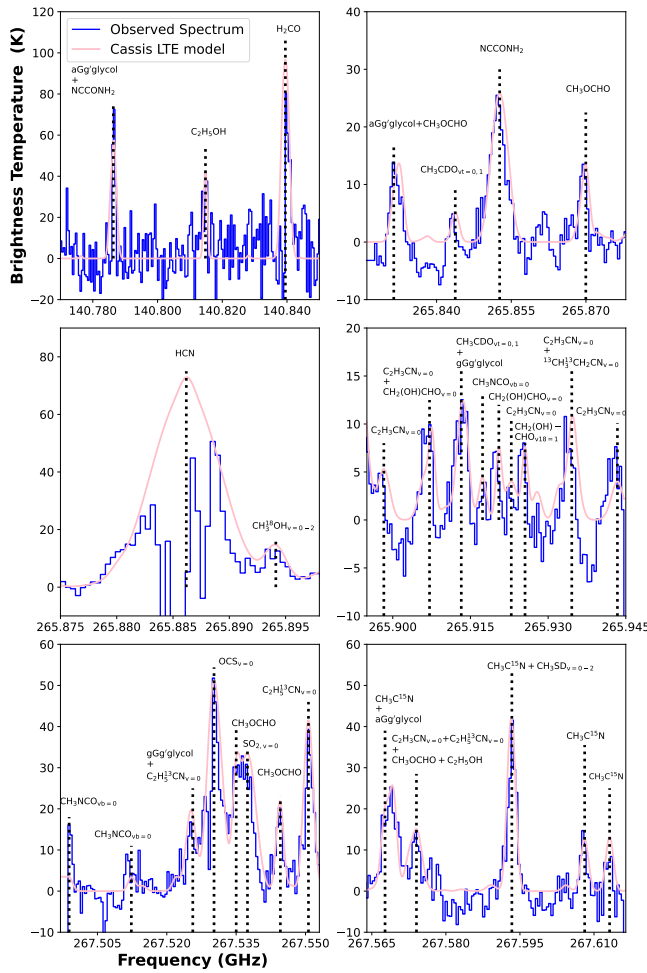
Figure 3.1: CASSIS models of the spectral lines in IRAS4A2 (pink) are compared with the observed spectra (blue) at frequencies where line emission is detected. The molecules are labeled in black

our CASSIS model of the lines. Additionally, Appendix A includes Table A.1, which provides detailed information on all identified molecular lines and their transitions, and Table A.2, which summarizes their morphologies and physical properties, including excitation temperatures and column densities.

The discovery of the numerous COMs around IRAS4A2 came as a surprise, especially when compared to the lack of emission lines around IRAS4A1, primarily attributed to the highly optically thick dust emission of the latter. Recent studies, such as De Simone et al. (2020), López-Sepulcre et al. (2017), and Guerra-Alvarado et al. (2024), have highlighted the differences in optical depth between the two sources. Despite the challenge in observing emission from IRAS4A1, analyzing the diverse species emanating from IRAS4A2 offers valuable insights into the early stages of Class 0 objects and the beginnings of protoplanetary disk formation.

Our IRAS4A2 CASSIS model confirmed the detection of four COMs: $C_2H_3CN_{v=0}$, $CH_2(OH)CHO$, CH_3OCHO, and $CH_3C^{15}N$. While we were unable to fully fit some of the emission around IRAS4A2, nearly all lines were covered within our frequency range. The aGa$'$ glycol line, while providing temperature and column density estimates, was consistently blended with other molecules. For $C_2H_5^{13}CN$, only one detection was made, but the model suggests the potential for two more if temperatures or densities around IRAS4A2 were higher. Finally, the higher frequency line of $CH_3NCO_{vb=0}$ is partially cut off in the frequency range, leading to underestimations of the associated excitation temperature and column densities. Despite comparable column densities with those found in López-Sepulcre et al. (2017) for different COMs, it has already been mentioned before that the high dust opacity in hot corinos results in underestimations of the abundances (De Simone et al. 2020).

3.3.2 Outflows, extended emission and compact emission in IRAS4A2

3.3.2.1 Outflows

We employed the code *bettermoments* for collapsing the concatenated spectral cube, generating moment maps of the outflows of the IRAS4A system (both components) and the emission lines around only IRAS4A2 (Teague & Foreman-Mackey 2018). For a comprehensive view of the large-

scale outflows, moment 0 and moment 1 images were generated for HCN,
$HCO^+_{v=0,1,2}$, and H_2CO using the short baseline data. We present these
in Figure 3.2, providing information about the spatial distribution and
velocity structures of these outflows.

3.3.2.2   Extended emission

Four lines were identified as tracers of more extended emission in the
concatenated data, each exhibiting its own distinct morphology. These
molecules include SO_2, HCN, H_2CO, and OCS. In Figure 3.3 we present the
moment 0 and 1 maps of these molecules, with white contours outlining
the continuum dust emission at Band 6. For these specific spectral lines,
we obtained position-velocity (P-V) diagrams to determine the nature of
the observed emission, whether it was driven by infall motion, Keplerian
rotation from a disk, or a rotating infalling flattened envelope. To analyze
this, we used CARTA. We extracted a perpendicular P-V cut along the
IRAS4A2 outflow region, specifically, perpendicular to the North-East (NE)
to the South-West (SW) direction of the outflow (29 deg, Chahine et al.
(2024)). After generating the fits file, we analyzed the image and manually
selected points to fit the emission using the following models:

For infall motion, we adopt

$$v_{\text{infall}}(r) = \sqrt{2} \cdot \sqrt{\frac{GM}{|r|}}, \qquad (3.1)$$

For Keplerian rotation, we use

$$v_{\text{Keplerian}}(r) = \sqrt{\frac{GM}{|r|}}, \qquad (3.2)$$

and for a rotating infalling flattened envelope, following the methodology
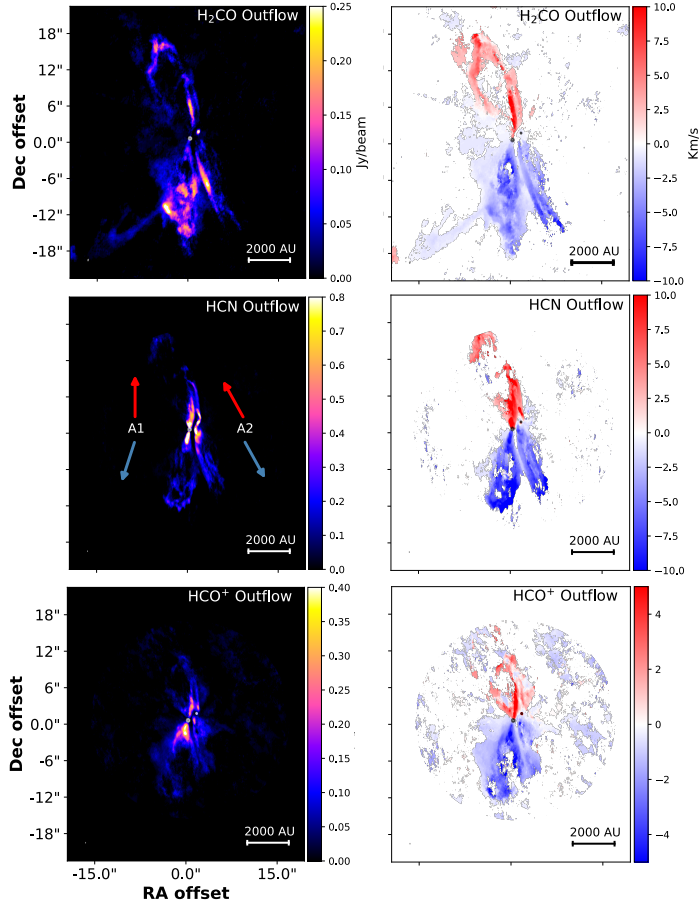
Figure 3.2: Integrated emission and velocity maps of the three main outflow tracers in our spectra: HCN, H_2CO, and HCO^+ generated using the short baseline line data for IRAS4A. The emission from the outflows of both sources, IRAS4A1 and IRAS4A2, is resolved and can be distinguished separately. In the figures, the dust continuum emission of IRAS4A1 and IRAS4A2 is outlined in small white contours, showing $5\,\sigma$ and $10\,\sigma$. The beam is drawn in the lower left part of each panel, 0.28"×0.17" for HCN and HCO^+ and 0.44"×0.28" for H_2CO. The red and blue arrows in the middle-left panel indicate the outflow directions of IRAS4A1 (left) and IRAS4A2 (right)(Chahine et al. 2024), respectively.

75
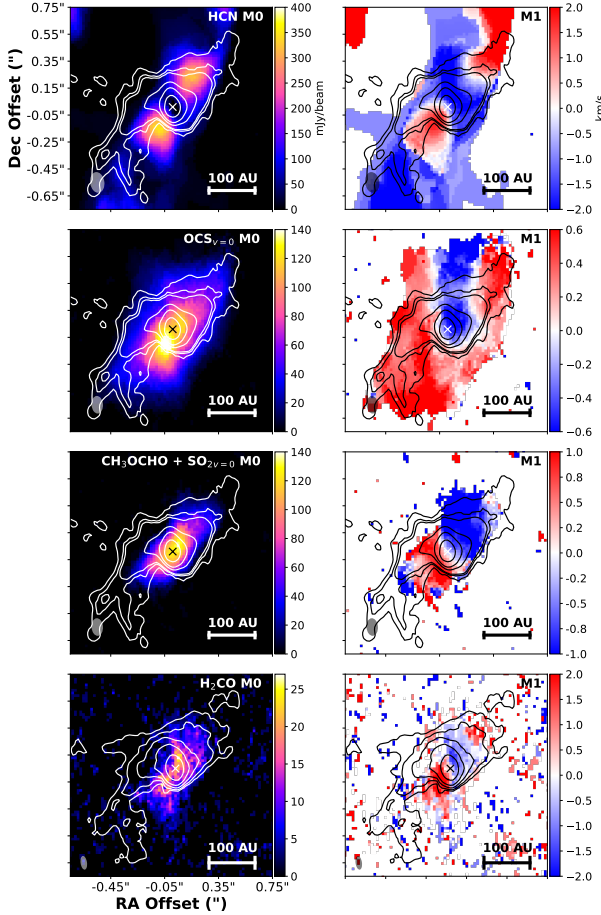
Figure 3.3: Integrated emission and velocity maps of SO_2, OCS, H_2CO and
HCN using the long+short baseline data. These molecular lines trace a
larger extended emission in IRAS4A2. We identified these features visually
from the spectra as the most intense and spatially extended emission
lines. The white and black contours represent the 6 to 60-σ levels of the
continuum emission from the ALMA Band 6 and Band 4 data, highlighting
the underlying dust distribution. The synthesized beam for all panels is
shown in the lower-left corner.

in Sakai et al. (2014) and Lee et al. (2017), we adopt

$$v_r(r) = -\sqrt{\frac{2GM}{r} - \frac{l^2}{r^2}},$$

(3.3)
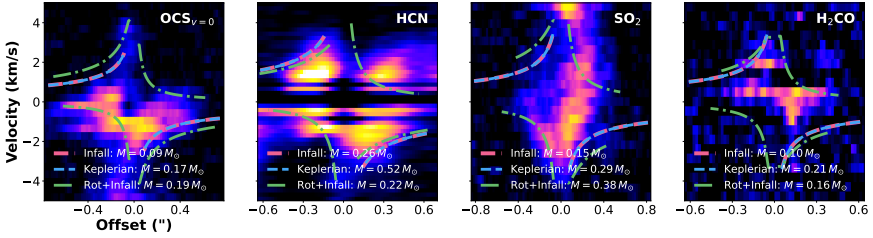
Figure 3.4: Position-velocity diagrams of SO_2, OCS, H_2CO, and HCN extracted along a cut perpendicular to the jet axis. The pink lines show the infall motion fit while the blue lines correspond to the Keplerian motion fit.

and,

$$v_\phi(r) = \frac{l}{r}, \tag{3.4}$$

where G is the gravitational constant, M is the mass of the central protostar, l is the specific angular momentum, and r is the distance from the central protostar.

In Figure 3.4, we present the P-V diagrams of the four extended molecules along with the Keplerian, infall, and the rotating infalling flattened envelope model fits, obtained using a non-linear least squares fitting procedure. While all four molecules tend to predict relatively low masses across the different models (see Figure 3.4), they exhibit variations in angular momentum, l, and centrifugal barrier (CB) radii, we show all this values in Table 3.2.

There are differences in the best fits of these four molecules that suggest different kinematic structures or physical origins. For OCS and H_2CO, the rotating infalling flattened envelope model reproduces the emission relatively well, although for H_2CO the model cannot reproduce the lower velocity emission. In contrast, for HCN and SO_2, the Keplerian and pure infall models better capture the observed emission patterns, but there is still significant emission that is not fit well by any of the models. Some possible contributing factors here are: absorption in certain velocity channels, that the molecules could be tracing multiple kinematic

components, or that the molecular lines fitted are blended with other
molecules, particularly for SO_2, which is blended with CH_3OCHO.

3.3.2.3   Compact emission

Several COMs, like CH_3OCHO, $CH_3CDO_{vt=0-1}$, $C_2H_3CN_{v=0}$, $CH_3NCO_{vb=0}$,
$CH_3{}^{18}OH_{v=0-2}$, and more, show much more compact emission, on scales
of 20 to 50 au with a range of morphologies (see Fig B.1). We catego-
rized these visually as the warm inner envelope (<20 au), disk (between
20 au and 40 au), and compact dust-absorbed emission (close to the
warm inner envelope) molecules, following Tychoniec et al. (2021). As an
illustration, Figure 3.5 displays the moment 0 maps generated by *better-
moments* for three representative molecules that were not blended with
any other line emission, showcasing the three regions they trace within
the IRAS4A2 system. In addition, Figure 3.5 includes the P-V diagram of
$CH_3CDO_{vt=0-1}$, taken along a cut perpendicular to the outflow axis, and
the moment 1 map of CH_3OCHO showing the velocity structure of this
particular molecule.

To investigate the spatial distribution of molecular emission in
IRAS4A2, we analyzed the emission radius using aperture photometry on
the moment 0 maps. We applied a signal-to-noise ratio (SNR > 5) thresh-

Table 3.2: Derived properties for each molecule under different dynamical
models. RIE stands for rotating infalling envelope.

Molecule	Model	M [$M_\odot$]	l [au·km·s^{-1}]	CB [au]
OCS	Keplerian	0.17 ± 0.07	–	–
	Infall	0.09 ± 0.03	–	–
	RIE	0.19 ± 0.04	38.5 ± 7.8	4.3 ± 2
HCN	Keplerian	0.52 ± 0.14	–	–
	Infall	0.26 ± 0.07	–	–
	RIE	0.22 ± 0.07	66.6 ± 13.5	11.2 ± 5.7
SO_2	Keplerian	0.29 ± 0.07	–	–
	Infall	0.15 ± 0.03	–	–
	RIE	0.38 ± 0.07	81.2 ± 10.8	9.87 ± 3.2
H_2CO	Keplerian	0.21 ± 0.04	–	–
	Infall	0.10 ± 0.02	–	–
	RIE	0.16 ± 0.03	44.4 ± 7.74	6.8 ± 2.7

old, masking all values below this limit, and then determined the 68% flux radius of the emission, r_{68}. We applied the methodology described in Appendix D of Podio et al. (2021), where we extract a cut perpendicular to the outflow axis going through the continuum peak to measure the spatial extent of the emission. We then assume the measured r_{68} corresponds to the FWHM/2 of the emission profile and deconvolve this value from the beam size to correct for beam smearing and avoid biases due to intensity variations across different molecular lines. Figure 3.6 shows the resulting radius plotted against the excitation temperature derived from CASSIS for molecules with available data. Using the same approach, Figure 3.6 also shows the measured emitting area of each molecule plotted against its respective upper energy levels.

It is important to note that many observed emission lines are blended with others, complicating the estimation of their emission radii and reducing accuracy. Furthermore, some molecular emission exhibits low signal-to-noise ratios or remains unresolved at the current spatial resolution. In these cases, we fixed the FWHM to the minimum beam size to avoid overestimating their spatial extent. Despite these concerns, we chose to proceed with the analysis, as even blended lines, when observed at high resolution, can still provide valuable insights into the chemical structure of young Class 0 objects like IRAS4A2. For a more precise determination of temperature and radius, multiple transitions of unblended molecular emission lines are required, as demonstrated in Frediani et al. (2025).

3.4 Discussion

3.4.1 Spatial scales of the dust and gas of IRAS4A2

3.4.1.1 Compact emission and the origin of the dust absorption

In IRAS4A2, the distributions of emission from COMs and other molecules appear to trace distinct physical processes. Identifying these at high
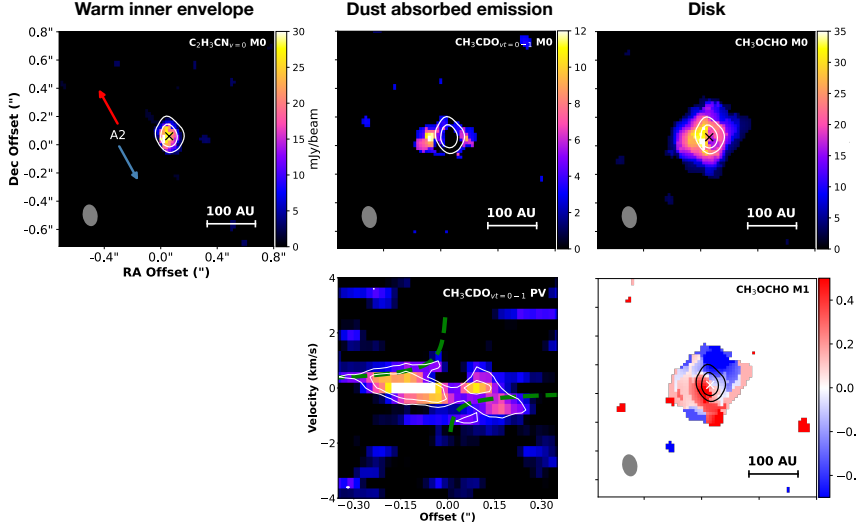
Figure 3.5: Integrated intensities of the three representative molecular lines that were not blended with any other, showcasing the three visually identified regions they trace within the IRAS4A2 disk: $C_2H_3CN_{v=0}$, $CH_3CDO_{vt=0-1}$ and CH_3OCHO. The top panels reveal three distinct morphologies of the compact emission: The left panel shows a warm inner envelope emission, the middle panel shows emission affected by dust absorption, and the right panel displays what seems to be a disk. The white contours show the $30\,\sigma$ to $60\,\sigma$ levels of the continuum emission, and the synthesized beams are indicated in the lower left corner of each image. The middle panel of the bottom row shows a P–V diagram of $CH_3CDO_{vt=0-1}$, extracted along a cut perpendicular to the outflow axis. The green dashed curve represents a Keplerian rotation model, while white contours indicate emission levels from $1.5\,\sigma$ to $3\,\sigma$, based on the Band 6 line data. The bottom right panel shows the moment 1 (M1) map of CH_3OCHO, indicating the velocity structure across the emitting region.

resolution can reveal key regions where planet-forming and disk-forming processes occur, as well as the sublimation temperatures that dictate where certain molecules transition from solid to gas. In particular, around IRAS4A2, molecular emission extends from the warm inner envelope ($\sim$ 20 au) to large-scale outflows ($\sim$ 5300 au).

As previously discussed, Figure 3.5 reveals different morphologies. Some molecules, such as $C_2H_3CN_{v=0}$ and $CH_3^{18}OH_{v=0-2}$, exhibit very compact emission below 20 au, smaller than the beam radius (0.065"), suggesting they remain still very unresolved. In particular, despite the uncertainties introduced by absorption, the Keplerian model provides a good fit to the $CH_3CDO_{vt=0-1}$ emission in Figure 3.5. Combined with the fact that the emission is not aligned with the outflow direction, this could suggest that $CH_3CDO_{vt=0-1}$ may serve as a reliable tracer of the disk itself. The emission from CH_3OCHO also appears not to be along the outflow direction. Its moment 1 map reveals a velocity gradient perpendicular to the outflow axis, with similar rotation to the flattened envelope, which could indicate that emission from this molecule traces the base of a disk wind or the disk. Further investigation of these two molecules may provide valuable information about the embedded disk and the early conditions enabling planet formation.

Some of these compact regions appear to trace a warm inner envelope or the innermost part of the IRAS4A2 system, as shown in Figure 3.6, especially given that emission from a couple of molecules remains unresolved. Moreover, the sizes of the emitting areas appear to correlate with lower values of upper-state energy levels. This trend suggests that higher-energy transitions trace warmer and more compact regions of the disk located closer to the central protostar. In contrast, lower-energy transitions probe a wider range of regions across the system. The most compact emission among these low upper state energy level lines could likely originate from colder regions in higher layers of the disk if the temperatures are lower there than in the mid-plane (Zamponi et al. 2021), and if they are effectively shielded from the protostar's radiation. Further supporting this interpretation is the observation that some compact and extended molecular emission still exhibits absorption features around IRAS4A2, whereas many others do not. This contrast implies that the emitting and sublimation regions of certain molecules may lie in higher but closer and warmer layers of the disk structure, where the dust optically thick
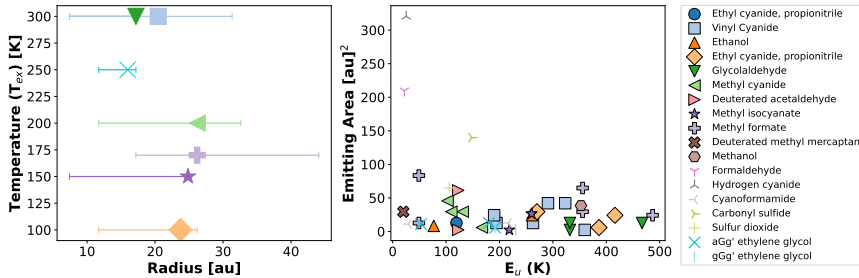
Figure 3.6: Left panel: Deconvolved radii of the emission plotted as a function of excitation temperature for the confirmed detected molecules in IRAS4A2. The error bars represent the minimum and maximum radii observed for all blended molecular lines, while the points indicate the median radius values. Right panel: The emission emitting area plotted against the upper state energy levels. Different colors and different figures represent emission from different molecules, as highlighted in the rightmost panel.

absorption appears to be now limited only to the innermost, with lower scale height regions. It is important to note that the protostellar envelope is normally related to an optically thick region at sub-mm wavelengths that absorbs the inner emission of Class 0/I objects (Galván-Madrid et al. 2018; Galametz et al. 2019) over a large extent. These absorption features have been observed and studied in other star-forming regions as well. For example, Lee et al. (2019) suggests that the absorption and reduction of line emission may be due to additional heating sources, which could be altering the temperature structure in the disk. This view comes from observations of systems experiencing accretion outbursts, similar to what has been observed in V883 Ori (Alarcón et al. 2024; Yamato et al. 2024). In the context of young stellar objects (YSOs), simulations by Baillié & Charnoz (2014) suggest that viscous heating could significantly impact the disk temperature beyond 20 au, affecting both the mid-plane and higher layers of the disk. Moreover, various hot spots have been identified in other protostellar sources, such as IRAS 16293-2422 A (Maureira et al. 2022). While the exact origin of these hot spots remains unclear, accre-

tion shocks, particularly those associated with infalling material along filamentary structures (streamers) from the extended envelope, are a primary candidate for generating such localized heating. As highlighted in Maureira et al. (2022), analyzing and identifying these diverse heating mechanisms is crucial for accurately modeling Class 0, and even Class I, protoplanetary disks as these systems have shown signs of late-stage accretion shocks (e.g., Garufi et al. 2022)

While additional heating processes may help explain some of the absorption features observed in IRAS4A2, an alternative explanation is continuum over-subtraction, an effect that arises when the optically thick continuum and the overlying gas have similar excitation temperatures, leading to absorption in the line profiles after subtraction of the continuum (see Nazari et al. 2024). Regardless of the underlying mechanism, this behavior is particularly clearly observed in the inner regions of IRAS4A2, very close to the central star. This behavior could suggest an evolutionary track, as previously mentioned, where strong absorption is now confined to the innermost regions for some molecules, in contrast to IRAS4A1 and some other regions, where much of its emission is still absorbed. This difference indicates that the optically thick dust or envelope has either dissipated in the outer regions, has become optically thin in most areas, or has shrunk and moved closer to the star and the mid-plane (as large dust grains are affected by settling and rapid radial drift). While these findings are intriguing, the absorbed emission may obscure critical details, preventing us from seeing the full picture with current observational capabilities. Furthermore, drawing conclusions about high-temperature and more compact molecular tracers remains challenging due to the limitations of both the CASSIS model and our spectral data (see Section 3.3), which explains the lack of a clear correlation between the excitation temperature and the radius of the emission.

3.4.1.2   Extended emission and its structure in IRAS4A2

Similarly, the extended emission in Fig.3.3 exhibits different morphologies, with some more complexity. First, H_2CO is a well-established tracer of the gas disk in YSOs (van't Hoff et al. 2020; Tychoniec et al. 2021). For $CH_3OCHO + SO_{2v=0}$, the emission would appear to originate from the same region as H_2CO, as they trace the same spatial extent, but it could also be tracing a potential disk wind (De Simone et al. 2024). Meanwhile, OCS appears to be an effective tracer of small grains, especially following the continuum emission bridge previously observed between IRAS4A1 and IRAS4A2 (as shown by the contours in Fig. 3.3 and in Guerra-Alvarado et al. (2024)). For both OCS and $SO_{2,v=0}$, it has been suggested that their extended emission in IRAS4A could originate from interactions between the outflow and the surrounding material (Taquet et al. 2020). The integrated emission maps further support the idea that both the grains and OCS are influenced by the S-shaped morphology of the IRAS4A2 outflow. A similar trend is observed for HCN, although in this case, its emission more clearly traces the disk continuum in the inner regions, suggesting it may be simultaneously tracing both the outflow and the gas component of the disk.

On the other hand, H_2CO and SO_2 do not fully align with the continuum emission. They are more compact and do not reach the outflow. This difference may arise from the fact that OCS transitions to the gas phase at lower temperatures than H_2CO and SO_2. Moreover, smaller dust grains, less affected by radial drift, tend to remain distributed over more extended colder regions, making OCS a suitable tracer of regions where only smaller dust grains are present. In contrast, the other two lines require higher temperatures, needing to be closer to the star to reach their sublimation temperatures, and therefore trace more evolved structures. Given this difference, one might expect that OCS and HCN trace a region with small dust grains, while H_2CO and SO_2 likely trace more inner structures, possibly those related to the gas disk. As shown in Fig. 3.4, however, while all

molecules yield reasonable mass estimates, both H_2CO and OCS emission is notably better fit by the rotational infalling envelope model. This commonality suggests that they may be tracing similar physical components. Nonetheless, it is important to note that the fit for H_2CO is not perfect and this interpretation may still involve uncertainties.

OCS, HCN, and H_2CO emission exhibits significant absorption by the dust continuum in the inner regions of the IRAS4A2 disk, near the warm inner envelope, with HCO^+ being completely absorbed.It is also worth noting that some of this molecular emission may be subject to self-absorption due to infalling material along the line of sight, which could either contribute to or even account for the observed absorption features, rather than dust absorption alone. In contrast, SO_2 shows little or no absorption compared to the other extended molecules, suggesting it may trace higher layers of the source, possibly the envelope. This behavior could indicate that HCN and H_2CO emission is likely tracing a more middle region, while HCO^+ emission, due to its strong absorption, may trace regions closer to the mid-plane of the source, where dust absorption from the shrinking envelope might still be significant. This stratification of molecular emission was also observed in HH212 by Lee et al. (2022), in IRAS4A2 by De Simone et al. (2024), and is consistent with findings in HD 163296, where emission from the same molecules were found to trace a similar vertical order (Paneque-Carreño et al. 2023).

In summary, the differences in characteristics between these molecules, such as H_2CO and SO_2 being more compact and not reaching the outflow, H_2CO and OCS having a common P-V diagram model and aligned masses, OCS, HCN, H_2CO, HCO^+ and SO_2 emission showing different absorption patterns, and the fact that HCN emission traces two components directly, suggest a discrepancy. These molecules may be tracing multiple components simultaneously, even at really small scales (in the warm inner envelope < 20 au) that vary in vertical distribution across radii and emission extent. Some of these interpretations, however, require further investigation to confirm which physical components these

molecules are actually tracing, and additional observations are needed
to disentangle the potential chemical or structural stratification within
IRAS4A2.

3.4.2 Accretion Shocks

OCS and SO_2 emission exhibits strong emission peaks that are outside of
the continuum disk region (see Fig. 3.3). This observed emission pattern
could be linked to shocks, as discussed in van Gelder et al. (2021), where
sulfur-bearing molecules serve as tracers for material flowing from the
envelope into the disk, likely originating from filaments formed by what
are commonly referred to as streamers. The formation of SO and SO_2
typically occurs towards the end of a shock, suggesting that their emission
is tracing such processes.

The origin of shocks in protostellar systems could be attributed to
various mechanisms, including outflows (Persson et al. 2012), accretion
shocks (Sakai et al. 2014; Garufi et al. 2022), or disk winds (Tabone et al.
2017). Notably, Artur de la Villarmois et al. (2022) identified SO_2 as the
most reliable tracer of accretion shocks, while Maureira et al. (2022) sug-
gested that such accretion shocks could be responsible for generating hot
dust spots. Furthermore, OCS and SO_2 emission appears too extended to
be solely associated with the envelope (Harsono et al. 2021).

In IRAS4A2, shocks are a plausible mechanism behind the observed
emission of OCS and SO_2. Identifying a single, dominant origin for these
shocks remains challenging, however, as they can arise in various contexts
within the system. A key distinction lies between accretion shocks, which
occur when infalling material decelerates upon impacting the disk surface,
generating localized heating, and outflow-induced shocks, which result
from the interaction between high-velocity outflows and the surrounding
envelope, often producing more spatially extended emission with broader
line profiles. Given the observations shown in Fig. 3.3, we propose that
the compact, localized intensity peaks seen in OCS and SO_2 integrated

emission maps are most consistent with accretion shocks. Meanwhile, the more extended and broader emission features may instead be associated with outflow-driven shocks (Taquet et al. 2020), reinforcing the idea that emission from these molecules could be tracing multiple components of the system.

It is difficult to determine from the P-V diagrams whether or not SO_2 exhibits the symmetric Keplerian signature expected from a disk wind (Tabone et al. 2017). If the absorption feature in the OCS P-V diagram is ignored, however, a pattern emerges, resembling the expected kinematics (broad and slower than the jet) of a rotating disk wind. This could explain why OCS appears to trace the smallest grains and suggests that it is simultaneously probing multiple components, such as accretion shocks and the disk wind. Nonetheless, determining the precise origin of these emissions remains challenging, and it is still possible that these lines trace a different component than assumed here.

Finally, a secondary peak of OCS emission is identified just outside the continuum contour image of IRAS4A1, aligned with the southern outflow. This finding is consistent with Taquet et al. (2020), who previously detected this molecule in the IRAS4A binary within the same region.

### 3.4.3 High mass star forming regions vs IRAS4A2

To understand the origin of hot corinos, and in particular the one associated with IRAS4A2, it is valuable to compare their chemical composition with those of hot cores of other star-forming regions and identify both similarities and differences. Hot corinos have been proposed as low-mass analogs of the hot cores observed in high-mass star-forming regions, sharing comparable chemical signatures despite differences in mass and environmental conditions. In Fig. 3.7, we compare the molecular abundances relative to methanol for the species detected in IRAS4A2 with those reported in both high-mass and low-mass star-forming regions. The column densities of methanol were taken from Frediani et al. (2025), who

accounted for optical depth effects in their analysis. When necessary, isotopologue abundances were adjusted to reflect the main species using solar system isotopic ratios from Wilson & Rood (1994).

From Fig. 3.7, IRAS4A2 appears to exhibit molecular abundances similar to those of high-mass star-forming regions such as AFGL4176 and Sgr B2, at least for the molecules where direct comparisons are possible. In the case of $C_2H_5{}^{13}CN$, where we predict a high molecular abundance, we suspect the CASSIS fitting may be unreliable because only one unblended line is clearly detected in our spectra. The remaining lines are either heavily blended or faint, introducing significant uncertainty in the total molecular abundance of this molecule.

When comparing the molecular inventory of IRAS4A2 with that of the high-mass star-forming region AFGL 4176 in Bøgelund et al. (2019), we find that both regions share many molecular species, though AFGL 4176 exhibits a greater number of transitions and lines, probably due to its higher mass. Interestingly, the only molecules not identified in AFGL 4176 are $NCC(O)NH_2$ and $CH_3NCO_{vb=0}$. $CH_3NCO_{vb=0}$, however, has been detected in other high-mass star-forming regions, including Orion KL and Sgr B2(N) (Cernicharo et al. 2016; Belloche et al. 2017), and a tentative detection of $NCC(O)NH_2$ has recently been reported in Sgr B2(N) (Li et al. 2024). This absence is not entirely surprising, as previous studies have noted that AFGL 4176 is more comparable to the low-mass protobinary system IRAS 16293 (Jørgensen et al. 2016) than to other high-mass sources like Sgr B2(N) and Orion KL. In contrast, IRAS4A2 appears more aligned with the latter, supporting the idea that hot corinos may be low-mass analogs of the hot cores in high-mass star-forming regions, sharing similar complex chemistry but on a smaller scale.

Regarding the spatial distribution of these molecules, we observe several similarities with AFGL 4176 Bøgelund et al. (2019). First, emission from transitions with lower upper-state energies appears to be more spatially extended than that from higher upper-state energy transitions. Additionally, emission from sulfur-bearing molecules is among the most ex-
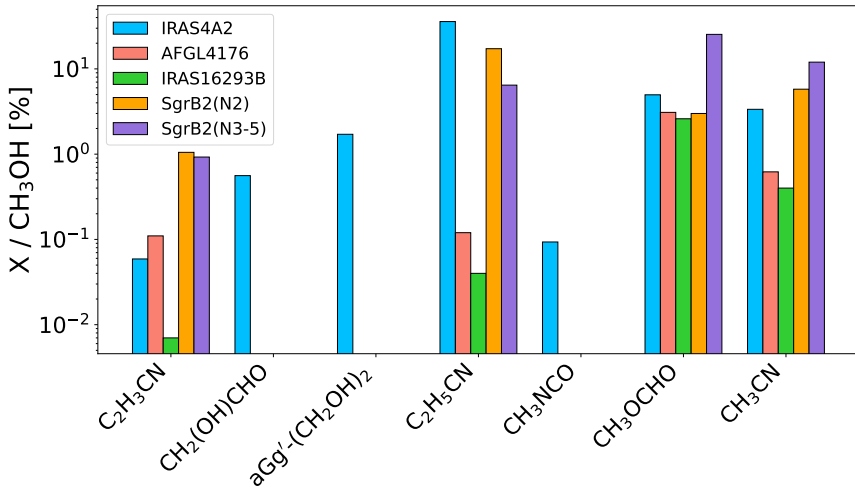
Figure 3.7: Normalized molecular abundance ratios relative to methanol, for the species detected in this work. The values are compared to those observed in both high-mass (AFGL4176 and SgrB2) and low-mass star-forming (IRAS16293B) regions.

tended compared to emission from other molecules, which aligns with detections in AFGL 4176 and our spatially resolved observations in IRAS4A2. Finally, we also observe a reverse trend with $C_2H_3CN_{v=0}$, like in AFGL 4176, with higher upper-state energy transitions corresponding to larger emitting areas. The reason for this reversal is still unclear and needs more investigation.

3.4.4 Outflows and misaligned velocity fields

The large-scale outflows observed in the IRAS4A region are from HCN, $HCO_{v=0,1,2}^+$, and H_2CO. These outflows extend to approximately 18" (~5300 AU). We resolve both outflows in all lines which allows for a clear distinction between the emission that originates from IRAS4A1 and IRAS4A2. We observed the distinctive S-shaped (observed in the moment 0 maps) pattern of the IRAS4A2 outflow, consistent with previous findings by Santangelo et al. (2015) and Chuang et al. (2021). This shape is

attributed to a misalignment between the initial core angular momentum
vector and the magnetic field. It is suggested that this misalignment can
happen if the Hall-induced magnetic field flips the angular momentum
vector between the flattened envelope and the circumstellar envelope
(Zhao et al. 2020a; Wurster et al. 2016).

By examining the moment 1 maps of the most extended molecular
emission, we find that the velocity fields in the inner regions of HCN,
H_2CO, OCS, and SO_2 are misaligned (flipped) with those of the outflow
(see Fig. 3.3). In contrast, for the more compact COMs, it is difficult to
determine a definitive rotation pattern due to SNR limitations. There are,
however, hints that these species may also exhibit a rotational direction
opposite to that of the outflow. This inversion of the velocity maps has
been previously observed in various disks before, such as VLA 1623B
(Ohashi et al. 2022), BHR71 (Tobin et al. 2019), and IRAS 16293-2422
(Zapata et al. 2013). Multiple origins for this inversion have been proposed,
including interaction with the outflow, hydrodynamical interaction with
the circumbinary disk, accretion shocks, and, more recently, material
accelerated by the disk wind as it crosses the plane of the sky (De Simone
et al. 2024). The exact cause of the inverted velocity gradient, however,
remains incompletely understood and requires further investigation.

3.5   Summary and conclusions

We have studied the hot corino of IRAS4A2 at high resolution using ALMA,
analyzing different spatial scales, from large-scale outflow-like emission
down to a small warm inner envelope (~20 au) emission. Our findings
indicate that:

- We confirm the detection of four complex molecules around
  IRAS4A2: $C_2H_3CN_{v=0}$, $CH_2(OH)CHO$, CH_3OCHO, and $CH_3C^{15}N$.

- Molecular emission appears to trace distinct regions within the
  IRAS4A2 system. Several species with small spatial extents and high

excitation temperatures are likely associated with a warm inner en-
velope or the innermost regions of IRAS4A2. In contrast, molecules
such as $CH_3CDO_{v_t=0-1}$ and CH_3OCHO may serve as effective tracers
of the disk structure, or a potential disk wind component. Further
studies are necessary to determine the potential of these molecules
for tracing the disk. If confirmed, however, these molecules could
serve as key tracers for studying the disk during its earliest stages,
when planet formation may have already begun.

- The extents of molecular emission observed in IRAS4A2 appear to
  correlate with lower upper-state energy levels. Given the incon-
  sistencies between absorption features, kinematic signatures (e.g.,
  P–V diagrams), and other observed properties, it is likely that ex-
  tended emission is tracing multiple components simultaneously.
  These components include the outflow, envelope, disk, warm inner
  envelope, and possibly accretion shocks, outflow shocks and the
  disk wind, reflecting the complex and dynamic environment of this
  young protostellar system.

- The emission peaks observed in the OCS and SO_2 moment 0 maps
  are more consistent with signatures typically associated with shocks,
  particularly accretion shocks, which may be responsible for heat-
  ing the dust in IRAS4A2. This hot dust could explain the promi-
  nent absorption features detected across the innermost regions
  of the spectra. In contrast, the more extended emission coming
  from the same molecules is better aligned with characteristics of
  outflow-driven shocks, suggesting that multiple shock mechanisms
  are contributing to the observed molecular emission.

- A comparison with high-mass star-forming regions such as AFGL
  4176, Sgr B2(N), and Orion KL shows that these sources share mostly
  the same molecular species. This commonality suggests that hot
  corinos do not exhibit significant differences in molecular composi-

tion regardless of mass or environment. Furthermore, the spatial distribution of these molecules appears to be similar across different sources, but more studies at high resolution are needed to confirm this.

- We resolved the large-scale ($\sim$ 5300 au) outflows of HCN, $HCO^+_{v=0,1,2}$, and H_2CO, distinguishing the outflows from IRAS4A1 and IRAS4A2. We confirm the previously reported S-shaped morphology and the inverted velocity gradient observed in this region, between the outflow emission and other components of IRAS4A2.

Appendix A: IRAS4A2 Molecules in spectra

Table A.1: Line characteristics

Molecule	Name	Transition	Rest Frequency (GHz)	A_{ij} (s^{-1})	E_u (K)	g_u
HCN	Hydrogen cyanide	(3-2)	265.88618	8.42e-4	25.52	21
$C_2H_3CN_{v=0}$	Vinyl Cyanide	(28 6 23-27 6 22)	265.9347953	1.49e-3	262.77	171
$C_2H_3CN_{v=0}$	Vinyl Cyanide	(28 8 21-27 8 20)(28 8 20-27 8 19)	265.9062054	1.44e-3	323.06	171
$C_2H_3CN_{v=0}$	Vinyl Cyanide	(28 9 19-27 9 18)(28 9 20-27 9 19)	265.943385	1.40e-3	359.59	171
$C_2H_3CN_{v=0}$	Vinyl Cyanide	(29 1 29-28 1 28)	265.9228854	1.56e-3	194.36	177
$C_2H_3CN_{v=0}$	Vinyl Cyanide	(28 7 21-27 7 20)	265.8982758	1.47e-3	290.78	171
$C_2H_3CN_{v=0}$	Vinyl Cyanide	(28 1 27-27 1 26)	267.5746326	1.59e-3	189.95	171
$CH_3CDO_{vt=0,1}$	Deuterated acetaldehyde	(14 4 10 0-13 4 9 0)	265.91423	6.12e-4	122.84	29
$CH_3CDO_{vt=0,1}$	Deuterated acetaldehyde	(14 4 10 2-13 4 9 2)	265.843748	6.05e-4	122.83	29
$CH_2(OH)CHO_{v=0}$	Glycolaldehyde	(34 3 31 0-34 2 32 0)	265.9076199	1.51e-4	331.78	69
$CH_2(OH)CHO_{v=0}$	Glycolaldehyde	(34 4 31 0-34 3 32 0)	265.9204834	1.51e-4	331.78	69
$CH_2(OH)CHO_{v18=1}$	Glycolaldehyde	(18 11 7 1-18 10 8 1)	265.9255426	2.20e-4	466.95	37
$CH_3^{18}OH_{v=0-2}$	Methanol	(16 3 14 0-16 2 15 0)	265.894132	9.63e-5	352.57	132
$NCC(O)NH_2$	Cyanoformamide	(23 18 5-23 17 6)(23 18 6-23 17 7)	265.852665	3.14e-4	216.70	47
$NCC(O)NH_2$	Cyanoformamide	(11 4 7-10 3 8)	140.7863341	4.88e-5	29.71	23
$gGg' - (CH_2OH)_2$	gGg' ethylene glycol	(26 11 16 1-25 11 15 0)	265.9131258	1.42e-4	230.25	371
$gGg' - (CH_2OH)_2$	gGg' ethylene glycol	(27 3 24 1-26 4 23 1)	267.5258901	2.10e-4	191.86	385
$aGg' - (CH_2OH)_2$	aGg' ethylene glycol	(26 4 23 1-25 3 22 1)	265.8326715	2.06e-4	180.49	371
$aGg' - (CH_2OH)_2$	aGg' ethylene glycol	(26 6 20 0-25 6 19 1)	267.5692918	4.29e-4	192.05	371
$aGg' - (CH_2OH)_2$	aGg' ethylene glycol	(13 4 10 1-12 4 9 0)	140.7865974	6.02e-5	53.05	243
$^{13}CH_3^{13}CH_2CN$	Ethyl cyanide, propionitrile	(12 9 4-13 8 5)(12 9 3-13 8 6)	265.9346645	5.15e-6	119.36	25
$C_2H_5^{13}CN_{v=0}$	Ethyl cyanide, propionitrile	(30 8 23-29 8 22)	267.5506331	1.48e-3	270.05	61
$C_2H_5^{13}CN_{v=0}$	Ethyl cyanide, propionitrile	(30 14 17-29 14 16)(30 14 16-29 14 15)	267.5740406	1.25e-3	416.15	61
$C_2H_5^{13}CN_{v=0}$	Ethyl cyanide, propionitrile	(30 13 18-29 13 17)(30 13 17-29 13 16)	267.5248859	1.30e-3	386.33	61
$CH_3NCO_{vb=0}$	Methyl isocyanate	(31 0 0 1-30 0 0 1)	265.917341	9.14e-4	218.36	63
$CH_3NCO_{vb=0}$	Methyl isocyanate	(31 3 28 0-30 3 27 0)	267.512332	9.12e-4	260.16	63
$CH_3NCO_{vb=0}$	Methyl isocyanate	(31 3 29 0-30 3 28 0)	267.498881	9.12e-4	260.15	63
CH_3OCHO	Methyl formate	(7 7 0 0-6 6 1 0)(7 7 1 0-6 6 0 0)	265.869967	4.35e-5	49.05	30
CH_3OCHO	Methyl formate	(7 7 0 2-6 6 0 2)	265.831401	4.35e-5	49.07	30
CH_3OCHO	Methyl formate	(24 1 23 3-23 1 22 3)	267.544467	2.85e-4	355.60	98
CH_3OCHO	Methyl formate	(24 2 23 3-23 2 22 3)	267.535013	2.85e-4	355.60	98
CH_3OCHO	Methyl formate	(22 15 7 5-21 15 6 5)	267.572288	1.55e-4	486.69	90
$CH_3C^{15}N$	Methyl cyanide	(15 1-14 1)	267.608	1.66e-3	109.91	62
$CH_3C^{15}N$	Methyl cyanide	(15 3-14 3)	267.567	1.60e-3	167.16	124
$CH_3C^{15}N$	Methyl cyanide	(15 2-14 2)	267.593	1.63e-3	131.38	62
$CH_3C^{15}N$	Methyl cyanide	(15 0-14 0)	267.613	1.66e-3	102.76	62
HCO^+	Formyl ion	(3 0 0-2 0 0)	267.557526	1.45e-3	25.68	7
$CH_3SD_{v=0-2}$	Deuterated methyl mercaptan	(3 2 1 1-2 1 1 1)	267.599	2.56e-5	19.95	7
$SO2_{v=0}$	Sulfur dioxide	(13 3 11-13 2 12)	267.5374512	1.51e-4	105.82	27
$OCS_{v=0}$	Carbonyl sulfide	(22-21)	267.530219	5.57e-5	147.67	45
H_2CO	Formaldehyde	(2 1 2-1 1 1)	140.839502	5.30e-5	21.92	15
C_2H_5OH	Ethanol	(12 3 10 2-12 2 11 2)	140.81481	1.67e-5	76.93	25
C_2H_5OH	Ethanol	(15 9 6 1-16 8 8 0)	267.5732224	7.63e-6	260.82	31

Table A.2: Morphology and physical properties

Molecule	Name	Morphology	T_{ex} [K]	N_{Sp} [cm^{-2}]	FWHM [Km/s]
HCN	Hydrogen cyanide	Outflow and cold flattened envelope	-	-	7.5
$C_2H_3CN_{v=0}$	Vinyl Cyanide	Disk, blend	300 ± 4	$1.77e15 \pm 0.01e15$	3
$C_2H_3CN_{v=0}$	Vinyl Cyanide	Disk, blend	300 ± 4	$1.77e15 \pm 0.01e15$	3
$C_2H_3CN_{v=0}$	Vinyl Cyanide	Warm inner envelope	300 ± 4	$1.77e15 \pm 0.01e15$	3
$C_2H_3CN_{v=0}$	Vinyl Cyanide	Upper side of the warm inner envelope	300 ± 4	$1.77e15 \pm 0.01e15$	3
$C_2H_3CN_{v=0}$	Vinyl Cyanide	Warm inner envelope	300 ± 4	$1.77e15 \pm 0.01e15$	3
$C_2H_3CN_{v=0}$	Vinyl Cyanide	Lower side of the warm inner envelope, blend	300 ± 4	$1.77e15 \pm 0.01e15$	3
$CH_3CDO_{vt=0,1}$	Deuterated acetaldehyde	Disk, blend	-	-	2
$CH_3CDO_{vt=0,1}$	Deuterated acetaldehyde	Absorbed at the warm inner envelope	-	-	2
$CH_2(OH)CHO_{v=0}$	Glycolaldehyde	Disk, blend	300 ± 3	$1.68e16 \pm 0.1e16$	1.5
$CH_2(OH)CHO_{v=0}$	Glycolaldehyde	Warm inner envelope	300 ± 3	$1.68e16 \pm 0.1e16$	1.5
$CH_2(OH)CHO_{v18=1}$	Glycolaldehyde	Warm inner envelope	300 ± 3	$1.68e16 \pm 0.1e16$	1.5
$CH_3^{18}OH_{v=0-2}$	Methanol	Warm inner envelope, part of disk	-	-	2.5
$NCC(O)NH_2$	Cyanoformamide	Disk	-	-	4
$NCC(O)NH_2$	Cyanoformamide	Warm inner envelope, blend	-	-	4
$gGg' - (CH_2OH)_2$	gGg' ethylene glycol	Disk, blend	-	-	2.5
$gGg' - (CH_2OH)_2$	gGg' ethylene glycol	Warm inner envelope, blend	-	-	2.5
$aGg' - (CH_2OH)_2$	aGg' ethylene glycol	Disk, blend	250 ± 3	$5.13e16 \pm 0.02e16$	2
$aGg' - (CH_2OH)_2$	aGg' ethylene glycol	Warm inner envelope, blend	250 ± 3	$5.13e16 \pm 0.02e16$	2
$aGg' - (CH_2OH)_2$	aGg' ethylene glycol	Warm inner envelope, blend	250 ± 3	$5.13e16 \pm 0.02e16$	2
$^{13}CH_3^{13}CH_2CN$	Ethyl cyanide, propionitrile	Disk, blend	-	-	2
$C_2H_5^{13}CN_{v=0}$	Ethyl cyanide, propionitrile	Disk	100 ± 0.3	$1.21e16 \pm 0.37e16$	2.5
$C_2H_5^{13}CN_{v=0}$	Ethyl cyanide, propionitrile	Warm inner envelope, blend	100 ± 0.3	$1.21e16 \pm 0.37e16$	2.5
$C_2H_5^{13}CN_{v=0}$	Ethyl cyanide, propionitrile	Warm inner envelope, blend	100 ± 0.3	$1.21e16 \pm 0.37e16$	2.5
$CH_3NCO_{vb=0}$	Methyl isocyanate	Absorbed at the warm inner envelope	150 ± 4	$2.8e15 \pm 0.05e15$	2
$CH_3NCO_{vb=0}$	Methyl isocyanate	Barely observed, warm inner envelope	150 ± 4	$2.8e15 \pm 0.05e15$	2
$CH_3NCO_{vb=0}$	Methyl isocyanate	Warm inner envelope	150 ± 4	$2.8e15 \pm 0.05e15$	2
CH_3OCHO	Methyl formate	Disk	170 ± 3	$1.49e17 \pm 0.09e17$	2
CH_3OCHO	Methyl formate	Disk, blend	170 ± 3	$1.49e17 \pm 0.09e17$	2
CH_3OCHO	Methyl formate	Disk	170 ± 3	$1.49e17 \pm 0.09e17$	2
CH_3OCHO	Methyl formate	Cold flattened envelope, blend	170 ± 3	$1.49e17 \pm 0.09e17$	2
CH_3OCHO	Methyl formate	Warm inner envelope, blend	170 ± 3	$1.49e17 \pm 0.09e17$	2
$CH_3C^{15}N$	Methyl cyanide	Disk	200 ± 6	$3.73e14 \pm 0.2e14$	2
$CH_3C^{15}N$	Methyl cyanide	Warm inner envelope, blend	200 ± 6	$3.73e14 \pm 0.2e14$	2
$CH_3C^{15}N$	Methyl cyanide	Warm inner envelope, blend	200 ± 6	$3.73e14 \pm 0.2e14$	2
$CH_3C^{15}N$	Methyl cyanide	Absorbed at the envelope	200 ± 6	$3.73e14 \pm 0.2e14$	2
$HCO^+_{v=0,1,2}$	Formyl ion	Outflow	-	-	-
$CH_3SD_{v=0-2}$	Deuterated methyl mercaptan	Disk	-	-	2
$SO2_{v=0}$	Sulfur dioxide	Cold flattened envelope, blend	-	-	4.5
$OCS_{v=0}$	Carbonyl sulfide	Cold flattened envelope	-	-	3.5
H_2CO	Formaldehyde	Outflow and cold flattened envelope	-	-	5
C_2H_5OH	Ethanol	Warm inner envelope	-	-	2.5
C_2H_5OH	Ethanol	Warm inner envelope, blend	-	-	2.5

Appendix B: IRAS4A2 Moment 0 maps
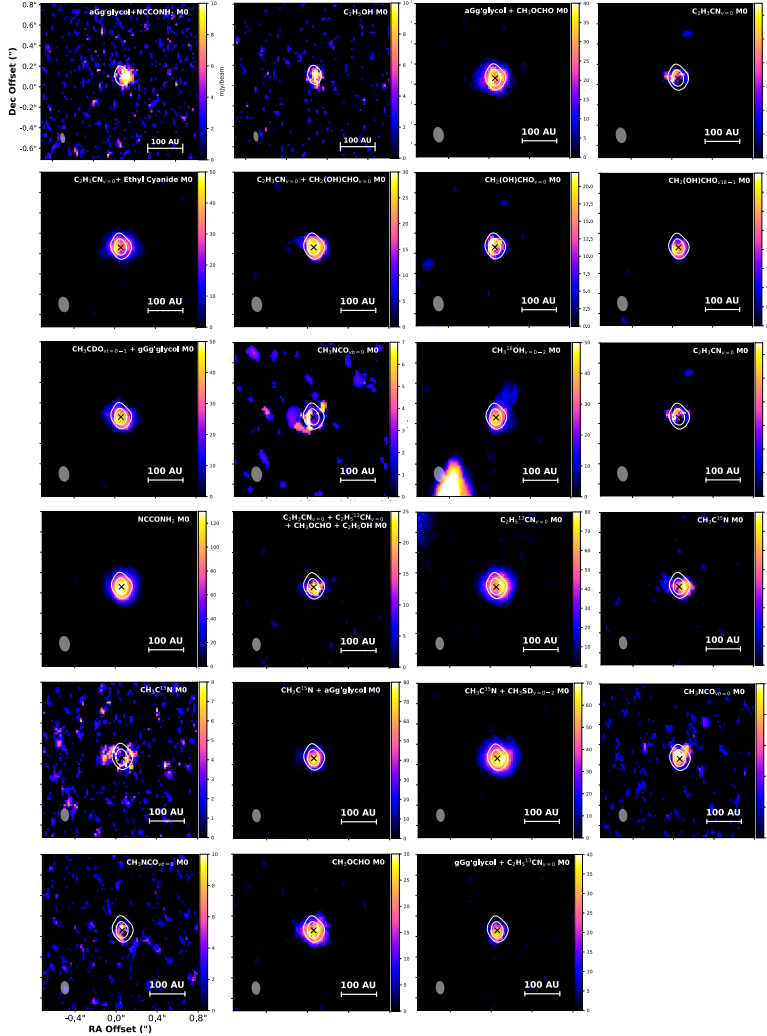
Figure B.1: Integrated emission (Moment 0) maps of all the remaining molecular lines identified in the ALMA Band 6 and Band 4 spectra of IRAS4A2.